Melting of Cu under hydrostatic and shock wave loading to high pressures

2008 J. Phys.: Condens. Matter 20 095220

(http://iopscience.iop.org/0953-8984/20/9/095220)

IOP PUBLISHING JOURNAL OF PHYSICS: CONDENSED MATTER

J. Phys.: Condens. Matter **20** (2008) 095220 (8pp) doi:10.1088/0953-8984/20/9/095220

Melting of Cu under hydrostatic and shock wave loading to high pressures

Qi An[1,5], Sheng-Nian Luo[2,6], Li-Bo Han[1], Lianqing Zheng[3] and Oliver Tschauner[4]

[1] School of Earth and Space Sciences, University of Science and Technology of China, Hefei, Anhui 230026, People's Republic of China
[2] Physics Division, Los Alamos National Laboratory, Los Alamos, NM 87545, USA
[3] School of Computational Science, Florida State University, Tallahassee, FL 32306, USA
[4] High-Pressure Science and Engineering Center and Department of Physics, University of Nevada, Las Vegas, NV 89154, USA

E-mail: sluo@lanl.gov

Received 19 November 2007, in final form 25 January 2008
Published 14 February 2008
Online at stacks.iop.org/JPhysCM/20/095220

Abstract

Molecular dynamics simulations are performed to investigate hydrostatic melting and shock-induced melting of single crystal Cu described by an embedded-atom method potential. The thermodynamic (equilibrium) melting curve obtained from our simulations agrees with static experiments and independent simulations. The planar solid–liquid interfacial energy is found to increase with pressure. The amount of maximum superheating or supercooling is independent of pressure, and is 1.24 ± 0.01 and 0.68 ± 0.01 at a heating or cooling rate of 1 K ps^{-1}, respectively. We explore shock loading along three main crystallographic directions: ⟨100⟩, ⟨110⟩ and ⟨111⟩. Melting along the ⟨100⟩ principal Hugoniot differs considerably from ⟨110⟩ and ⟨111⟩, possibly due to different extents of solid state disordering. Along ⟨100⟩, the solid is superheated by about 20%, before it melts with a pronounced temperature drop. In contrast, melting along ⟨110⟩ and ⟨111⟩ is quasi-continuous, and premelting (∼7%) is observed.

(Some figures in this article are in colour only in the electronic version)

1. Introduction

Experimental determination of a melting curve in the Mbar pressure regime has remained a great challenge; static (quasi-static) techniques such as piston–cylinder, multi-anvil press and diamond anvil cell are normally limited to pressures below 1 Mbar (100 GPa) [1, 2]. As a complement, planar shock wave loading (uniaxial strain) may probe melting above 1 Mbar [3, 4] by utilizing simultaneous compression and heating. However, a shocked solid undergoes non-hydrostatic loading even when its supported shock state is hydrostatic. Thus, the solid relieves its deviatoric stresses via structural changes, for instance solid state disordering. Development of such disordering is in principle minimized under hydrostatic conditions commonly assumed in static experiments. Another drastic difference between static and shock loading is timescale: it is about 1–100 s in the former and 10^{-9}–10^{-6} s in the latter as regards both heating and strain rates. First-order phase transitions such as melting and crystallization are highly rate dependent [5]. Such differences between static and shock experiments have motivated us to examine shock-induced melting of single crystal Cu with respect to its thermodynamic melting curve using molecular dynamics (MD) simulations.

Previously, shock-induced melting of face-centered-cubic (fcc) solids including Cu has been briefly addressed by Bringa *et al* [6] and in more detail by Ravelo and co-workers [7] using MD simulations. Different melting pressure and superheating along three crystallographic directions were reported [7]. Jeong and Chang [8] carried out hydrostatic 'Hugoniot' simulations, which do not have direct bearing on the anisotropy in shock response. A self-consistent comparison between hydrostatic and shock melting is still lacking, and it is highly desirable to characterize in detail shock melting in a system described by accurate interatomic

[5] Present address: California Institute of Technology, Pasadena, CA 91125, USA.
[6] Author to whom any correspondence should be addressed.

potentials. Here we present our MD simulations and analysis on Cu using a widely used, accurate embedded-atom method (EAM) potential, for which high pressure melting under hydrostatic and shock wave loading has not been explored or sufficiently characterized. For hydrostatic melting, we determine the equilibrium melting curve of Cu up to 300 GPa, and characterize the maximum superheating and supercooling, thermodynamic properties and solid–liquid interfaces at high pressures. For shock wave loading on single crystal Cu along ⟨100⟩, ⟨110⟩ and ⟨111⟩, we characterize the Hugoniot states in terms of stress tensor, temperature, and shock and particle velocities; the characteristics of incipient and complete melting are analyzed based on the Hugoniots and equilibrium melting curve. Section 2 presents briefly the methodology on MD simulations, followed by results and discussion (section 3). Section 4 summarizes our main conclusions.

2. Methodology

We adopted the widely used EAM potential by Mishin *et al* [9] to describe the atomic interactions in Cu. MD simulations employed a standard parallel package IMD [10]. For loading under hydrostatic conditions, we applied the constant-pressure–temperature ensemble and three-dimensional (3D) periodic boundary conditions. Temperature (T) was controlled with a Hoover thermostat [11], and pressure (P) with isotropic volume scaling [10]. An initially perfect fcc solid was subjected to incremental compression to 300 GPa along the 300 K isotherm, yielding initial configurations for subsequent isobaric heating and cooling. The solid was heated incrementally into the liquid regime at a fixed pressure, and the temperature increment was 20 or 100 K. Similarly, incremental cooling of liquid was performed to achieve crystallization. The time step for integrating the equation of motion was 1 fs. At each temperature and pressure, the run duration was 50 000 steps. System sizes of 4000, 8000 and 62 500 atoms were used in hydrostatic simulations. Previous simulations on the system sizes ranging from 10^3 to 10^6 atoms have revealed negligible size effect [12].

Planar shock wave loading simulations were performed following the methods detailed in [13, 14]. A shock wave propagates into a single crystal Cu target when it impacts an infinitely massive wall or it is impacted by a Cu flyer plate, achieving a supported high pressure and high temperature shock state. Simulations with both methods yielded the same results. Three loading directions (the x-axis) were explored: ⟨100⟩, ⟨110⟩ and ⟨111⟩, for which ⟨010⟩ and ⟨001⟩, ⟨$\bar{1}$10⟩ and ⟨001⟩, and ⟨$\bar{1}$01⟩ and ⟨1$\bar{2}$1⟩ were chosen for the y- and z-axes, respectively. The aspect ratio for the target (x:y:z) ranged from about 6:1:1 to 10:1:1, and the system sizes were on the order of 10^5 atoms. Larger system sizes were not explored systematically because the results from these system sizes are consistent with previous simulations using much larger systems [6]. The simulation cell lengths along the x-axis and the simulation durations (5–10 ps) were sufficient for achieving supported shock states. Periodic boundaries were applied along the y- and z-axes, and free surface(s) or a fixed boundary was adopted along the x-axis. For a given particle velocity (u_p), the corresponding shock velocity (u_s) was obtained from velocity or stress profiles at different times (t). Physical quantities such as T and stresses are averages within the steady shock region. The stress tensor σ_{ij} ($i, j = x, y, z$) was calculated via averaging the atomic stress tensors, which were in turn determined with the decomposed virial method [15].

3. Results and discussion

3.1. Hydrostatic loading: the melting curve, superheating and supercooling, and the solid–liquid interfaces

Under incremental heating at a given pressure with 3D periodical boundaries, an initially perfect single crystal Cu is superheated and melts at a critical temperature (T_+). Similarly, a Cu liquid is supercooled and freezes at T_-. Such incremental heating and cooling yield hysteresis loops typical of first-order phase transitions, for example the volume–temperature (V–T) loop shown in figure 1(a). However, the equilibrium melting temperature T_m is neither of $T_\pm$. To determine $T_m(P)$, we adopted two well established methods: the solid–liquid coexistence (two-phase) method [17] and the superheating–supercooling hysteresis method [18, 19]. For the latter, $T_m = T_+ + T_- - \sqrt{T_+T_-}$. In the two-phase method, T is varied until the solid is in equilibrium with the liquid in a solid–liquid mixture with planar interfaces and T_m is deduced from the interface velocity [12] or the potential energy [20]. The agreement between these methods has been demonstrated for Lennard-Jonesium, Al and NaCl at high pressures, and Cu at ambient pressure [12, 19, 20]. The simulation details for both methods are thus omitted here.

As an example of the agreement between these two methods at high pressures, we utilized both methods to obtain T_m at 200 GPa. Given $T_+ = 6750 \pm 50$ K and $T_- = 3750 \pm 50$ K, T_m of 5470 ± 40 K was obtained from the hysteresis method, in excellent agreement with 5450 ± 50 K from the two-phase method. Due to its relative simplicity, we adopted the values of T_m from the hysteresis method for high pressures (figure 2). Fitting with the Simon equation, $T_m(P) = T_{m0}(P/a + 1)^b$, yields $a = 15.37$ GPa and $b = 0.53$ with the ambient value T_{m0} fixed at 1325 ± 20 K [12] (1% RMS error). Overall, the current melting curve agrees with previous experiments [1, 2] and independent *ab initio* and EAM-type MD calculations [21–23] (figure 2). (Other simulation results are not included in figure 2 for clarity, and details can be found in [21].) Along the melting curve $T_m(P)$, the volume of solid and liquid, and the heat of fusion (ΔH_m, figure 3(a)) at T_m were also obtained. Given ΔH_m and T_m, the entropy of melting was also obtained as a function of pressure; e.g., it is about $1.13R$ at zero pressure where R is the gas constant; it decreases monotonically with pressure and approaches approximately a constant of $0.84R$ at pressures above 200 GPa.

Both superheating and supercooling in the solid ↔ liquid phase transitions have been well documented in experiments and simulations [4, 18, 24]. The maximum superheating and supercooling achieved in our MD simulations are defined as $\theta_\pm \equiv T_\pm/T_m$ for a given pressure. For isobaric melting and

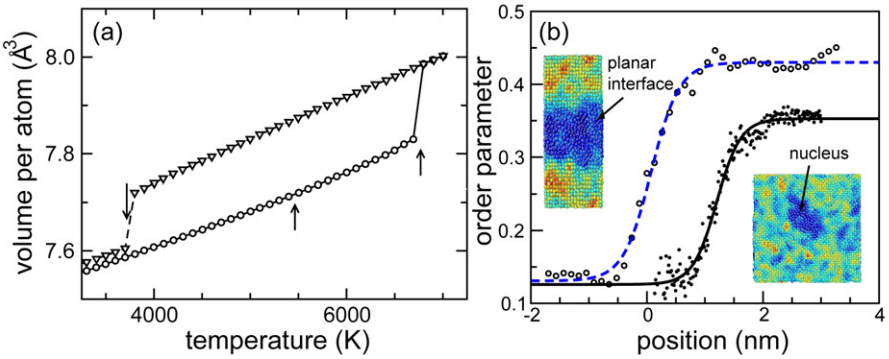

Figure 1. Melting of Cu at 200 GPa. (a) The V–T hysteresis loop upon incremental heating (circles) and cooling (triangles). Arrows denote T_-, T_m and T_+ from left to right, respectively. (b) The atomic configurations (insets) of the solid–liquid mixtures with planar interfaces (5400 K and $t = 60$ ps), and curved interfaces (6800 K and $t = 9.3$ ps), and corresponding order parameter profiles. The profile for the latter refers to the largest nucleus. Visualization of atomic configuration adopted AtomEye [16].

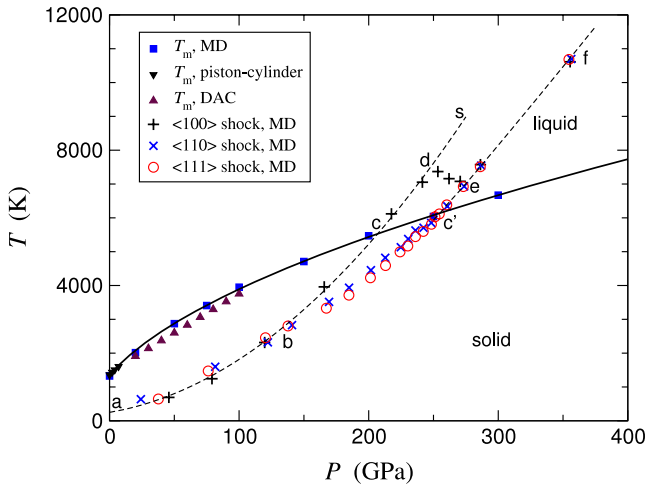

Figure 2. Static melting temperature from experiments (triangles [2] and inverted triangles [1]) and our MD simulations, and shock temperature of single crystal Cu shocked along ⟨100⟩, ⟨110⟩ and ⟨111⟩. The solid curve denotes the equilibrium melting curve fitted with the Simon equation. Dashed curves are schematic. Melting occurs at 238–265 GPa in shock wave experiments on polycrystalline Cu [3].

crystallization, $T_\pm$ and T_m were obtained as a function of P, allowing for examination of the pressure dependence of $\theta_\pm$. For homogeneous nucleation in Cu, $\theta_\pm$ can be regarded as constant with respect to pressure, and are 1.24 ± 0.01 and 0.68 ± 0.01, respectively, at a heating/cooling rate of about 1 K ps^{-1} (figure 3(b)). These results are nearly the same as Al [18], the Lennard-Jones system [19] and NaCl [20] with cubic crystal structures.

We have examined in detail the solid–liquid interfaces in Cu at ambient pressure [12], and it would be interesting to explore the interfacial characteristics at high pressures including interfacial energy (γ) and interface profile. For a given atom i, the ordering or disordering of an atom with respect to its nearest neighbors can be quantified with the local order parameter ($\bar{\psi}_i$) introduced by Morris and Song [12, 25]. The insets of figure 1(b) are two examples of atomic configuration visualized with $\bar{\psi}_i$ for solid–liquid mixtures showing planar and curved interfaces. (The areas indicated by arrows are most disordered.) The planar interface is from the two-phase simulation, and the curved interface from a snapshot during homogeneous nucleation and growth at 200 GPa. Averaging $\bar{\psi}_i$ within a rectangular slab for the former and within a spherical shell for the latter yields 1D order parameter profiles, $\Psi(z)$ and $\Psi(r)$, respectively. Such profiles can be described with a sigmoidal function (figure 1(b)), for example,

$$\Psi(z) = \Psi_\mathrm{liq} + \frac{\Psi_\mathrm{sol} - \Psi_\mathrm{liq}}{2}\left[1 + \tanh\left(\frac{z - z_0}{2w}\right)\right], \qquad (1)$$

for the planar interface. Here z denotes the distance, z_0 is the center of the interface and w represents a characteristic length scale of the interface. Fitting to the simulation results yields $w = 2.4$ and 2.1 Å for the planar and curved interfaces, respectively, comparable to their counterparts at ambient pressure and lower temperatures (about 2.3 and 2.7 Å) [12]. Note that it is not desirable to make literal comparison as these values evolve dynamically.

Cu is a model fcc metal; its solid–liquid interfacial energy γ at high pressures is of particular interest but has rarely been explored with experiments or simulations. The interfacial energy depends on the curvature of the solid–liquid interface [26], and it is difficult to calculate γ from simulations or to measure it directly from experiments. (See [12, 27] for a more detailed discussion.) Recently, we developed the superheating–supercooling hysteresis method for evaluating the planar interfacial energy, γ_∞, from $T_\pm$ and ΔH_m, that can be readily obtained from simulations. This method is based on the superheating–supercooling systematics [18, 27], which relate superheating/supercooling ($\theta_\pm$) and heating/cooling rate (Q) to the dimensionless nucleation barrier β as

$$\beta = (A_0 - b\log_{10} Q)\theta_\pm(1 - \theta_\pm)^2, \qquad (2)$$

where $\beta \equiv 16\pi\gamma_\infty^3/(3k_\mathrm{B}T_\mathrm{m}\Delta H_\mathrm{m}^2)$, k_B is the Boltzmann's constant, $A_0 = 59.4$, $b = 2.33$ and Q is normalized to 1 K s^{-1}. It follows that

$$\gamma_\infty = \left(\frac{3}{16\pi}\beta k_\mathrm{B}T_\mathrm{m}\Delta H_\mathrm{m}^2\right)^{1/3}. \qquad (3)$$

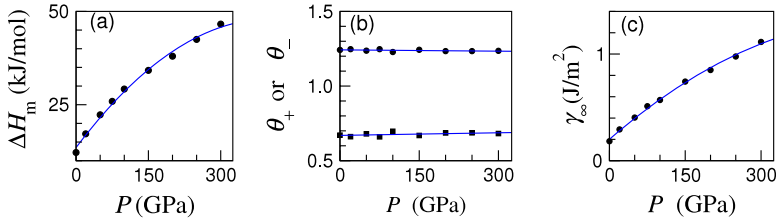

Figure 3. Heat of fusion (ΔH_m; (a)), superheating and supercooling ($\theta_\pm$; (b)), and planar interfacial energy (γ_∞; (c)) as a function of pressure obtained from current MD simulations (dots). The curves represent polynomial fittings to the simulations (P is in GPa): (a) $\Delta H_m = 13.5 + 0.17P - 2.1 \times 10^{-4} P^2$ kJ mol^{-1}; (b) $\theta_+ = 1.24 - 3.0 \times 10^{-5} P$ and $\theta_- = 0.67 + 5.9 \times 10^{-5} P$; (c) $\gamma_\infty = 0.2 + 4.1 \times 10^{-3} P - 3.6 \times 10^{-6} P^2$ J m^{-2}.

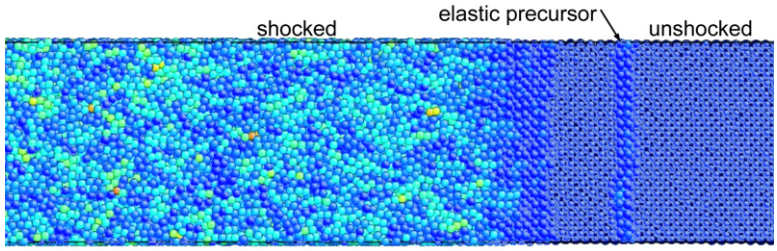

Figure 4. Atomic configuration of Cu single crystal shocked along ⟨110⟩ visualized with σ_{xx} ($u_p = 2.9$ km s^{-1} and $t = 3$ ps).

Here ΔH_m is normalized to the average volume of the liquid and solid at T_m. The accuracy of this method has been demonstrated for Lennard-Jonesium, NaCl and H_2O [20, 27]. Given $T_\pm$ and ΔH_m, we thus obtained γ_∞ as a function of pressure for planar interfaces (figure 3). γ_∞ increases with pressure as seen in the water–ice system and Lennard-Jonesium [27]. If γ for a spherical interface of radius r is desired, $\gamma = \gamma_\infty/(1 + 2w/r)$ [26], where both w and r can be estimated from the order parameter profile (figure 1(b)) [12].

3.2. Shock wave loading on single crystal Cu along ⟨100⟩, ⟨110⟩ *and* ⟨111⟩

Single crystal Cu solids were shock-loaded to various high pressure and high temperature states from ambient conditions, and underwent solid state structural changes (e.g. plastic deformation) as well as shock-induced melting at sufficiently high pressures.

For planar shock loading above the elastic limit ($u_p > 0.75$ km s^{-1}), a plastic wave of higher σ_{xx} may be preceded by an elastic precursor of lower σ_{xx}. The two-wave structure is manifested in, for instance, the atomic configurations and the particle velocity, temperature or stress wave profiles (figures 4 and 5). Due to the elastic and plastic anisotropy, the elastic precursors differ drastically along ⟨100⟩, ⟨110⟩ and ⟨111⟩. The elastic and plastic waves are of similar speed and thus indistinguishable from the wave profiles for the ⟨100⟩ shock. While the two waves are well separated for ⟨110⟩ and ⟨111⟩ shocks at low stresses, the elastic wave is characterized by large spatial fluctuations along ⟨110⟩. The elastic wave persists for the ⟨110⟩ shock to high shock strength (e.g. $u_p = 3$ km s^{-1}), where it is overtaken by the plastic wave for the ⟨111⟩ shock. Similar observations were made previously [6]. Both u_s and u_p of the elastic shock are less well defined as compared to

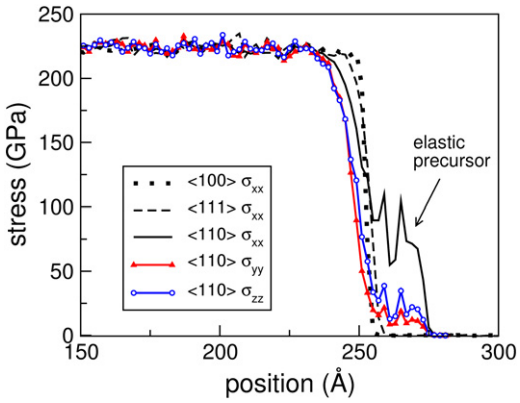

Figure 5. Stress profiles in shocked single crystal Cu ($u_p = 3.0$ km s^{-1} and $t = 4$ ps).

the plastic shock, normally with a well defined shock front and plateau (supported shock). For a plastic shock with prescribed u_p, u_s was obtained from wave profiles within 1%. Shock temperature was obtained from the temperature profiles in the supported plastic shock regime with an uncertainty of 50–100 K.

For shock loading along the x-axis, σ_{xx}, u_s and u_p presumably satisfy the Hugoniot jump condition for momentum,

$$\sigma_{xx} = \rho_0 u_s u_p. \tag{4}$$

As an independent check against the above equation, the stress tensor σ_{ij} behind the shock front was obtained as an averaged atomic stress tensor over the supported shock regime from kinetic energy, virial and volume of individual atoms [15]. σ_{xx} for the plastic wave so obtained agrees with the Hugoniot jump condition within 0.1%–0.5% for u_p above 1.5 km s^{-1},

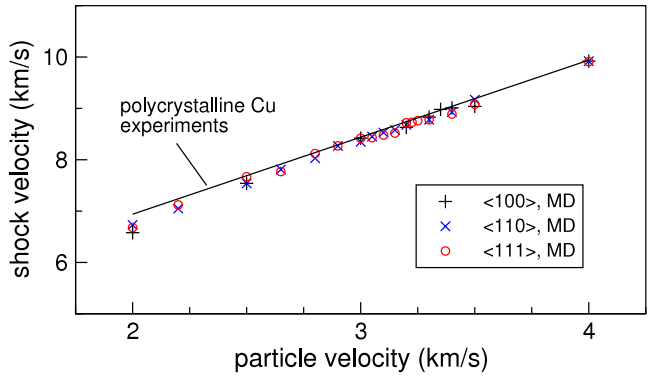

Figure 6. The u_s–u_p relation for shocked single crystal Cu (MD) and for polycrystalline Cu (a linear fitting to experiments [28]).

the regime relevant to shock melting. A hydrostatic condition means $\sigma_{xx} = \sigma_{yy} = \sigma_{zz}$. Above the elastic limit, the shock state is not necessarily under hydrostatic conditions because of material strength; for example, σ_{xx} (81.5 GPa) differs from σ_{yy} and σ_{zz} by ∼9% for the ⟨111⟩ shock with $u_p = 1.5$ km s^{-1}. σ_{xx} as deduced from equation (4) also suffers from less accuracy in u_s at low pressures. Thus, the pressure was calculated from σ_{ij} as $P = \frac{1}{3}(\sigma_{xx} + \sigma_{yy} + \sigma_{zz})$ for all the shock states instead of assuming $P = \sigma_{xx}$ obtained from equation (4).

Since the main purpose of the current work is high pressure melting, the details of plasticity and material strength will be presented elsewhere. The following discussion refers to the plastic wave because of its pronounced shock heating and relevance to melting, and to the equivalent hydrostatic pressure in order to make a meaningful comparison of shock melting with hydrostatic melting.

Shock-induced melting may have signatures of different sensitivity in shock temperature and the u_s–u_p relation. In the T_H–P curve, the latent heat of melting may induce a kink or other deviations from the solid part of the Hugoniot. (Subscript H refers to the Hugoniot state.) Shock melting may yield similar features in the u_s–u_p curve because the solid and liquid differ in the thermomechanical properties, and the P–T conditions change upon melting. Direct shock temperature measurements are still not feasible for opaque solids such as Cu; the measurements at the sample–window interface represent a reshocked or released state and are susceptible to uncertainties in thermal conductivities of both target and window materials [29]. The experimental u_s–u_p data in both solid and liquid regimes can be described with a single linear relation, $u_s = C_0 + su_p$ with $C_0 = 3.94$ km s^{-1} and $s = 1.5$ for polycrystalline Cu [28]. No clear indication of melting is identified on the u_s–u_p plot within experimental uncertainties. Shock sound speed (release wave) is another indicator of melting, and such measurements suggest that Cu melts at 232–265 GPa [3], consistent with indirect shock temperature measurement [30].

The u_s–u_p relations are shown in figure 6 for the ⟨100⟩, ⟨110⟩ and ⟨111⟩ shock simulations. To compare with experimental result for polycrystalline Cu ($C_0 = 3.94$ km s^{-1} and $s = 1.5$), fittings with the linear u_s–u_p relation were performed on the MD results between u_p of 2 km s^{-1} and 4 km s^{-1} including all three orientations: $C_0 = 3.57 \pm 0.06$ km s^{-1} and $s = 1.59 \pm 0.02$ without fixing either of them; $C_0 = 3.85 \pm 0.05$ km s^{-1} with s fixed at 1.5; and $s = 1.47 \pm 0.02$ with C_0 fixed at 3.94 km s^{-1}. While it is still unclear how to construct a polycrystalline Hugoniot from single crystal Hugoniots, the fittings to the MD results for single crystal Cu are in remarkable agreement with the experimental data (not shown in figure 6). Similar to the experimental observation on polycrystalline Cu, it is difficult to distinguish definitively the linear solid and liquid regimes in our simulations. By closely examining the slopes and offset, we roughly identify the partial melting regime as 3.3–3.5 km s^{-1}, 2.9–3.2 km s^{-1} and 3.0–3.3 km s^{-1} (in terms of u_p) for ⟨100⟩, ⟨110⟩ and ⟨111⟩, respectively.

The T_H–P curves manifest distinct features for shock loading along ⟨100⟩, ⟨110⟩ and ⟨111⟩ (figures 2 and 7). Overall, the T_H–P curves are similar for ⟨110⟩ and ⟨111⟩, and deviate from the ⟨100⟩ curve around 135 GPa. Along ⟨100⟩, the signature of melting (a kink) is pronounced on the T_H–P curve, which shows well defined solid, liquid and mixed phase (solid–liquid) regimes. Nonetheless, the solid and liquid regimes can only be distinguished from the change in the T_H–P slope and the mixed phase regime is narrower and difficult to identify for ⟨110⟩ and ⟨111⟩ (figure 7). Starting with ⟨100⟩, we identify the onset and completion of melting, determine the nature of melting (first order versus continuous melting) and quantify the extent of superheating or premelting for all three orientations.

Let (P_i, T_i), $i = 1, 2, 3$, be defined at d, e and s in figure 2 for ⟨100⟩, respectively, and $P_2 = P_3$. (P_1, T_1) represents the onset of melting, and (P_2, T_2), the completion of melting. The mixed phase regime is the states along the Hugoniot between (P_1, T_1) and (P_2, T_2). (P_3, T_3) is a fictitious state and denotes the extrapolated solid state corresponding to (P_2, T_2). These states can be defined similarly for ⟨100⟩ and ⟨111⟩.

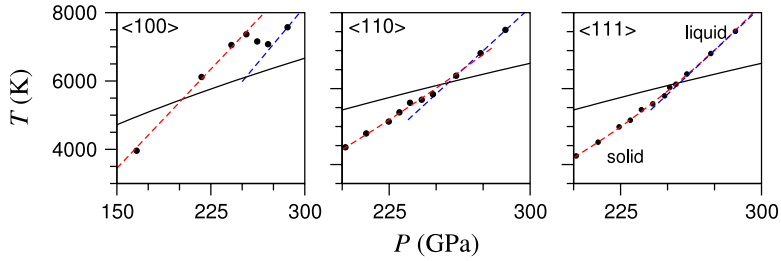

Figure 7. Temperature of shocked single crystal Cu (enlarged plot of figure 2). The solid curve denotes the melting curve, and the dashed curves linear or quadratic fittings to the solid and liquid states.

Table 1. Shock-induced melting of single crystal Cu. Numbers in parentheses denote estimated uncertainties.

Orientation	⟨100⟩	⟨110⟩	⟨111⟩
Onset of melting			
P_1 (GPa)	252(4)	236(4)	236(6)
T_1 (K)	7370(160)	5560(120)	5400(180)
T_m (K)	6100(120)	5900(120)	5900(120)
$\theta_{+,H}$	1.21(0.05)	0.93(0.04)	0.92(0.04)
Completion of melting			
P_2 (GPa)	274(5)	248(5)	254(5)
T_2 (K)	7030(200)	5800(150)	6040(150)
T_3 (K)	8240(200)	5940(150)	6100(150)
L_H (kJ mol^{-1})	33.9(7.8)	3.9(5.9)	1.7(5.9)

At the onset of melting, the solid reaches the critical temperature state where melting has to occur; the isobaric superheating (positive or negative) is characterized with a reduced temperature

$$\theta_{+,H} \equiv \left.\frac{T_1}{T_m}\right|_{P_1}. \tag{5}$$

$\theta_{+,H} < 1$ indicates negative superheating (premelting). At the completion of melting, the adiabatic heat of fusion on a Hugoniot (L_H) is defined with (P_2, T_2, E_2) and (P_3, T_3, E_3), and is not necessarily at the solid–liquid equilibrium. Here E denotes the internal energy. For an adiabatic process from state 3 to state 2, the total energy is conserved during shock-induced phase transition ($E_2 = E_3$), and the temperature drops from T_3 to T_2 due to the latent heat of fusion if we neglect the volume term. (Note that the equilibrium heat of fusion ΔH_m is defined at the same P and T for both solid and liquid, and is different from L_H.) Thus, a reasonable estimate of the latent heat of shock melting is

$$L_H \approx \bar{c}_p(T_3 - T_2)\Big|_{P_2=P_3}, \tag{6}$$

where $\bar{c}_p$ denotes the average heat capacity of the solid and liquid at the same pressure. In the pressure range 200–300 GPa, the heat capacity is about 27 J K^{-1} mol^{-1} for the solid and 29 J K^{-1} mol^{-1} for the liquid from hydrostatic simulations, and $\bar{c}_p$ is ∼28 J K^{-1} mol^{-1}.

The solid, liquid and mixed phase regimes on the T_H–P curves (figure 7) were identified with constraints from the u_s–u_p relations (figure 6). The solid and liquid states on the T_H–P curves were fitted with linear or quadratic relations, which were extrapolated to higher or lower pressures (figure 7). The results and estimated uncertainties are listed in table 1 for the pressure and temperature at the onset and completion of melting as well as superheating and the latent heat of fusion. The pressure ranges for melting observed in our MD simulations are consistent with shock wave experiments on polycrystalline Cu [3].

At the onset of melting, the Cu single crystal shocked along ⟨100⟩ undergoes about 21 ± 5% superheating, comparable to the value (24 ± 1%) observed for hydrostatic melting of perfect crystals. A similar amount of superheating has been inferred in shock experiments on alkali halides and silica [4, 31, 32]. In sharp contrast, the Cu single crystal experiences premelting of 7–8% (±4%) when shocked along ⟨110⟩ and ⟨111⟩. For comparison, [7] reported nearly zero superheating for Cu along ⟨100⟩ but more pronounced premelting (15–20%) along ⟨110⟩ and ⟨111⟩. Another appreciable difference is the nature of phase transition (first order versus continuous): while melting along ⟨100⟩ is obviously first order, it is quasi-continuous along ⟨110⟩ and ⟨111⟩ as seen from figures 2 and 7. The considerably smaller latent heat (table 1) for ⟨110⟩ and ⟨111⟩ also indicates the nature of (quasi-)continuous phase change.

In order to reveal the main structure features of the shocked solid that are probably related to the anisotropy in shock-induced melting of Cu, we calculated the radial distribution function, RDF, within the supported shock regime (figure 8(a)). The solid undergoes different degrees of disordering before transitioning into a liquid state when shocked along different orientations: this solid state disordering is much more pronounced along ⟨110⟩ and ⟨111⟩ compared to ⟨100⟩. (Upon complete melting, the liquids from shock loading along different orientations and those from hydrostatic melting are very similar or the same in structure and thermodynamic properties.) For example, shock loading along ⟨110⟩ to 122 GPa and 2300 K yields a highly disordered solid as seen from the RDF and atomic configuration (figures 8(a) and (b)). The RDF of this solid is nearly identical to that of the liquid at 120 GPa and 3000 K obtained from hydrostatic simulations (not shown). We used 3000 K instead of 2300 K since the liquid crystallized at about 2900 K and 120 GPa. Such structure similarity is further confirmed by the agreement in their broad coordination number distributions (figure 8(c)). At higher pressures, the RDFs of the disordered solid (202 GPa) and the liquid at complete melting (287 GPa) are also nearly identical to the liquids obtained from hydrostatic melting at similar pressures. However, the solid from shock loading along ⟨100⟩ retains the long range order: the fcc lattice is preserved in the atomic configuration (not shown) and the RDF (e.g. at 120 and 218 GPa, figure 8(a)) displays pronounced peaks compared to the solids from the ⟨110⟩ shocks or liquids, in particular at long distances. These features are similar to the solid under hydrostatic compression (not shown) at similar pressures and temperatures.

The above analysis suggests that the anisotropy in solid state disordering induces that in shock-induced melting of single crystal Cu. Previously, we have demonstrated that solid state amorphization precedes continuous melting in stishovite [33]. A disordered solid structurally similar to a liquid (as in the cases of ⟨110⟩ and ⟨111⟩ shocks) will invoke a lower energy barrier and less latent heat upon melting than those retaining crystalline order (as in the cases of ⟨100⟩ shock and hydrostatic compression). These observations indicate two distinct mechanisms for melting in shocked single crystal Cu: while the thermal cause is predominant for ⟨100⟩, as in the hydrostatic melting, solid state disordering plays a key role in melting induced by shock along ⟨110⟩ and ⟨111⟩ and is complemented by shock heating.

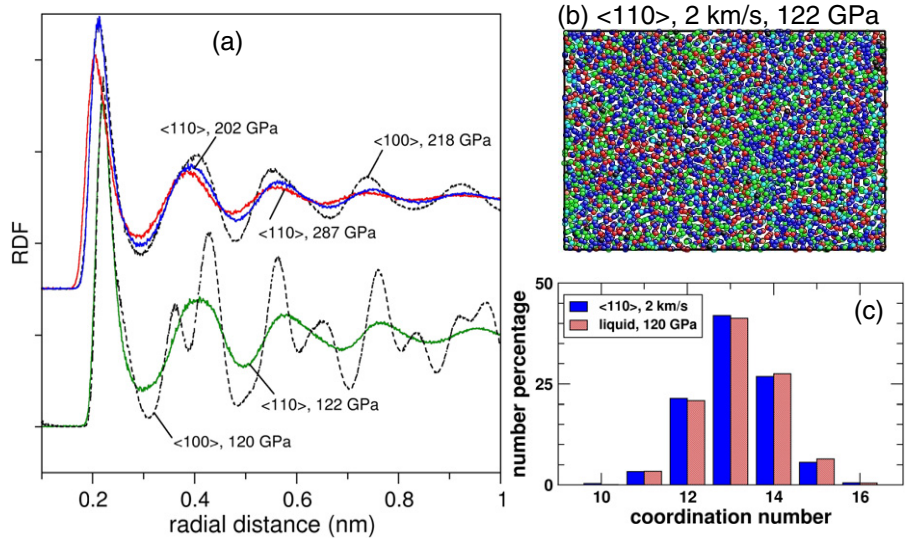

Figure 8. (a) Comparison of shock state radial distribution function (RDF) for ⟨100⟩ and ⟨110⟩. (b) A cross section of the atomic configuration for shock loading to 122 GPa along ⟨110⟩. (c) Number percentage of atoms versus coordination number. A cutoff distance of 0.3 nm was used for calculating the coordination number.

Defects are a well known factor contributing to lowering melting temperature (e.g. premelting) [34]. Well defined defects such as stacking faults and twins in fcc solids [6, 35] are only found at pressures below ∼50 GPa for Cu. In the pressure range relevant to shock melting, possible defects are point defects, but they are ill defined for strongly disordered solids as in the cases of ⟨110⟩ and ⟨111⟩ shocks and for liquids. The broad coordination number distributions (e.g. figure 8(c)) cannot properly characterize 'point defects' in disordered solids and liquids. Thus, solid state disordering is the dominant cause for premelting and quasi-continuous melting induced by the ⟨110⟩ and ⟨111⟩ shocks.

While the complex shock phenomena are interesting by themselves, the above observations pose challenges to their accurate interpretation and direct comparison with hydrostatic measurements as regards e.g. phase boundaries. The nonhydrostaticity and nonequilibrium phase transitions (e.g. superheating) are present to a lesser extent in static experiments than in shock wave loading, so caution should be exercised for a meaningful comparison.

4. Conclusions

The thermodynamic (equilibrium) melting curve of Cu described by the EAM potential of Mishin *et al* has been obtained up to 300 GPa with the solid–liquid coexistence method and the superheating–supercooling hysteresis method from hydrostatic MD simulations, and these two methods yield similar results. The simulated melting curve agrees with experiments and independent MD simulations based on different potentials and *ab initio* calculations. The maximum superheating and supercooling under hydrostatic loading are independent of pressure, and are 1.24 ± 0.01 and 0.68 ± 0.01 at a heating or cooling rate of 1 K ps^{-1}, respectively; these values are typical of fcc solids and alkali halides. The solid–liquid interfacial energy for the planar interface increases monotonically with pressure; e.g., it is about 0.18 J m^{-2} at zero pressure and 1.1 J m^{-2} at 300 GPa. The characteristic scale for the interface thickness is about 2.4 Å at 200 GPa for the planar interface, comparable to its counterpart at zero pressure.

Under planar shock wave loading of single crystal Cu, the behavior of shock-induced melting is anisotropic. For the ⟨100⟩ shock, melting is first order with about 20% superheating. Quasi-continuous melting and premelting (about 7%) have been observed for the ⟨110⟩ and ⟨111⟩ shocks. Such observations could be explained by the anisotropy in solid state disordering when single crystal Cu responds to shock loading along different orientations. These results underscore the necessity of considering anisotropy, kinetics and solid state disordering when interpreting shock wave experiments.

Acknowledgments

We have benefited from valuable discussions with D Tonks, E Bringa, Y Wang and Z-H Sun. One of the authors (SNL) is supported by the Inertial Confinement Fusion program (S Batha) and the Laboratory Directed Research Development program (LDRD-DR-20060021, A Koskelo) at LANL. LANL is under the auspices of the US Department of Energy under contract No. DE-AC52-06NA25396. QA and LBH acknowledge the support from NSF of China Grants No. 40537033 and 40425005 (S Ni). LZ is grateful for W Yang's support. OT acknowledges the support by the NNSA cooperative agreement No DE-FC88-01NV14049.

References

[1] Akella J and Kennedy G C 1971 *J. Geophys. Res.* **76** 4769
[2] Japel S, Schwager B, Boehler R and Ross M 2005 *Phys. Rev. Lett.* **95** 167801
[3] Hayes D, Hixson R S and McQueen R G 2000 *Shock Compression of Condensed Matter—1999* vol CP505, ed M D Furnish, L C Chhabildas and R S Hixson (Melville, NY: American Institute of Physics) p 483

[4] Luo S N and Ahrens T J 2004 *Phys. Earth Planet. Inter.* **143/144** 369
[5] Christian J W 1965 *The Theory of Transformation in Metals and Alloys* (New York: Pergamon)
[6] Bringa E M, Cazamias J U, Erhart P, Stolken J, Tanushev N, Wirth B D, Rudd R E and Caturla M J 2004 *J. Appl. Phys.* **96** 3793
[7] Ravelo R, Holian B L, Germann T C and Lomdahl P 2005 *Shock Compression of Condensed Matter—2005* vol CP845, ed M D Furnish, M Elert, T P Russell and C T White (Melville, NY: American Institute of Physics) p 270
[8] Jeong J W and Chang K J 1999 *J. Phys.: Condens. Matter* **11** 3799
[9] Mishin Y, Mehl M J, Papaconstantopoulos D A, Voter A F and Kress J D 2001 *Phys. Rev.* B **63** 224106
[10] Stadler J, Mikulla R and Trebin H R 1997 *Int. J. Mod. Phys.* C **8** 1131
[11] Hoover W G 1985 *Phys. Rev.* A **31** 1695
[12] Zheng L Q, An Q, Xie Y, Sun Z H and Luo S N 2007 *J. Chem. Phys.* **127** 164503
[13] Holian B L and Lomdahl P S 1998 *Science* **280** 2085
[14] Strachan A, Çağın T and Goddard W A III 2001 *Phys. Rev.* B **63** 060103
[15] Lutsko J F 1989 *J. Appl. Phys.* **65** 2991
[16] Li J 2003 *Modelling Simul. Mater. Sci. Eng.* **11** 173
[17] Morris J R, Wang C Z, Ho K M and Chan C T 1994 *Phys. Rev.* B **49** 3109
[18] Luo S N, Ahrens T J, Çağın T, Strachan A, Goddard W A III and Swift D C 2003 *Phys. Rev.* B **68** 134206
[19] Luo S N, Strachan A and Swift D C 2004 *J. Chem. Phys.* **120** 11640
[20] An Q, Zheng L Q, Fu R S, Ni S D and Luo S N 2006 *J. Chem. Phys.* **125** 154510
[21] Vocadlo L, Alfe D, Price G D and Gillman M J 2004 *J. Chem. Phys.* **120** 2072
[22] Belonoshko A B, Ahuja R and Johansson B 2000 *Phys. Rev.* B **61** 3838
[23] Moriarty J A 1986 *Shock Waves in Condensed Matter* ed Y M Gupta (New York: Plenum) p 101
[24] Kelton K F 1991 *Solid State Phys.* **45** 75
[25] Morris J R and Song X 2002 *J. Chem. Phys.* **116** 9352
[26] Tolman R C 1949 *J. Chem. Phys.* **17** 333
[27] Luo S N, Strachan A and Swift D C 2005 *Modelling Simul. Mater. Sci. Eng.* **13** 321
[28] Marsh S P 1980 *LASL Shock Hugoniot Data* (Berkeley, CA: University of California Press)
[29] Luo S N and Swift D C 2007 *Physica* B **388** 139
[30] Dai C, Tan H and Geng H 2002 *J. Appl. Phys.* **92** 5019
[31] Boness D A and Brown J M 1993 *Phys. Rev. Lett.* **71** 2931
[32] Lyzenga G A, Ahrens T J and Mitchell A C 1983 *J. Geophys. Res.* **88** 2431
[33] Luo S N, Zheng L Q and Tschauner O 2006 *J. Phys.: Condens. Matter* **18** 659
[34] Porter D A and Easterling K E 2001 *Phase Transformations in Metals and Alloys* (Cheltenham: Nelson Thornes Ltd)
[35] Luo S N, Zheng L Q, An Q and Zhao S 2006 *Int. J. Mod. Phys.* C **17** 1551